a reprint from Applied Optics

High-aspect-ratio line focus and plasma production using a random phase plate

M. Desselberger, L. Gizzi, V. Barrow, J. Edwards, F. Khattak, S. Viana, O. Willi, and C. N. Danson

The use of rectangular-element random phase plates to generate a line focus is described. Photographic records of the resultant focus are presented and compared with theoretical calculations made by using an interference code. Good agreement is found. The code is used to investigate possible design modifications to produce a more square-topped line focus. A 12-ps Raman-shifted KrF ($\lambda = 0.268$ μm) laser pulse is used in combination with such plates to produce a laser plasma. The plasma conditions are extensively characterized by using time-resolved extreme UV spectroscopy and a pinhole camera, and their suitability for x-ray laser applications is discussed.

I. Introduction

Recently a number of optical techniques for smoothing laser beam focal spots have been developed as part of the program to improve the uniformity of direct-drive inertial confinement fusion implosions. These methods include random phase plates[1] (RPP's), induced spatial incoherence[2] (ISI), and smoothing by spectral dispersion.[3] Smoother focal spots result from the elimination, or at least reduction, of the coherence of the laser light. To date square and circular smoothed focal spots have been produced. In many situations, however, other focal spot profiles are required. These include x-ray laser systems[4] where line foci are required and laser etching applications that require various focal spot geometries, depending on the application. We describe the production of line foci by using modified RPP's but stress that the same modification procedure could be used to produce almost any focal spot geometry. Apart from the versatility and simplicity of the development that we describe here, there are important additional advantages over more traditional methods of achieving noncircular focal spots (for example, off-axis multielement systems and cylindrical lenses). The use of random phasing to produce the desired profile provides a greater degree of control over optical aberrations in the system and is generally more efficient in terms of energy loss. A further advantage of particular importance to short-pulse (< 10 ps) applications where the spatial extent of the pulse is small (10 ps ≡ 3 mm) is the fact that random phasing introduces only a negligible delay (maximum delay = $\lambda/2 \ll$ pulse length) across the line focus. Off-axis optics by comparison introduce a delay that, in many cases of interest (including x-ray laser-type line foci with high aspect ratios), is significant with respect to the pulse length. In this paper images of the focal spots obtained with such modified RPP's are presented along with numerical simulations and possible design improvements. Furthermore, measurements demonstrating the feasibility of using these RPP's for x-ray laser-type systems are presented.

II. Numerical Model for Focal Spot Simulation

To model the intensity profile produced by different smoothing techniques an interference code was written. The code solves the two-dimensional, complex Kirchhoff diffraction integral in the Fresnel approximation[5] [Eq. (1)] and allows variation of the axial distance parameter z_i to select different planes throughout the focal region. A fast-Fourier-transform algorithm is used to solve the integral. RPP and ISI behavior is modeled by using a Gaussian statistics routine to generate appropriate phase fronts. The code was used to investigate the effect on the focal spot intensity profile of broadband laser light, RPP, ISI (and the effectiveness of these techniques in non-far-field focusing conditions, $z_i < f$), and inten-

M. Desselberger, L. Gizzi, V. Barrow, J. Edwards, F. Khattak, S. Viana, and O. Willi are with The Blackett Laboratory, Imperial College of Science, Technology and Medicine, Prince Consort Road, London SW7 2BZ, UK; C. N. Danson is with the Rutherford Appleton Laboratory, Chilton, Didcot, Oxon OX11 0QX, UK.

Received 6 August 1991.
0003-6935/92/193759-08$05.00/0.

sity and phase variations in the incident beam. A full account of the results, including analysis of the degree of uniformity achieved and of the mode spectrum present in each case, is published elsewhere.[6]

$$E(x_i, y_i) = C(x_i, y_i, z_i)\mathrm{FT}[E(x_0, y_0)\exp[i\varphi(x_0, y_0)] \times \exp[i\mathbf{k}(x_0^2 + y_0^2)/2][(f - z_i)/2fz_i]], \quad (1)$$

where (x_0, y_0) are the coordinates in the input plane, i.e., just before the lens,
(x_i, y_i) are the coordinates in the focal plane,
$\mathbf{k}(=2\pi/\lambda)$ is the wave vector,
z_i is the distance of the focal plane from the image plane ($z_i = f$ is tight focus),
f is the focal length of the lens,
FT[ ] represents the two-dimensional complex Fourier transform with respect to (x_0, y_0),
$C(x_i, y_i, z_i) = (K/\lambda z_i)\exp(ik[z_i + [(x_i^2 + y_i^2)/2z_i]])$,
K is a real constant (dependent on the units used in the calculation),
$E(x_o, y_o)$ $[=I_o(x_o, y_o)^{1/2}]$ is the electric-field amplitude in the input plane,
$\varphi(x_o, y_o)$ is the phase front in the input plane $(0 < \varphi < 2\pi)$.

[The far-field intensity distribution is simply $I(x_i, y_i) = E(x_i, y_i)^2$.]

The RPP phase front is modeled by generating an array of randomly distributed phase shifts that take a value of either 0 or π. This is not quite the same as, but is equivalent to, the original RPP concept,[1] where random shifts with values anywhere between 0 and π were used. The advantage of the binary-type phase plates is that production by lithographic techniques is simplified. All the RPP's that are produced for the experimental investigations described here were of the binary type. The input plane electric-field function $E(x_o, y_o)$ was found to be well approximated by a square top-hat function (as determined by the microdensitometry of an image of the near-field beam). Typical values for distortions introduced by the laser system were included additionally in the input plane phase $[\varphi(x_o, y_o)]$ and electric-field $[E(x_o, y_o)]$ functions.

III. Experimental Measurements of the Focal Spot

Phase plates with rectangular $(a \times b)$ elements were produced by a lithographic technique that is described in detail elsewhere.[7] When used in combination with an ordinary spherical lens, they produce a line focus with an aspect ratio of a:b (provided that the performance of the illumination system is diffraction-limited). The SPRITE short-pulse, high-power KrF laser system[8] of the Science and Engineering Research Council Central Laser Facility was used as the source in the investigations that are presented here because of its suitability to the production of hot, high-density plasmas, as described in Section V. Magnified images of the focal spots produced were recorded on Ilford HP5 film at several planes thoughout focus by means of an equivalent plane camera. Typical average irradiances achieved with the 12-ps, $\lambda = 1/4$ μm pulse were $\simeq 10^{14}$ W cm^{-2}.

Figure 1(a) shows a microdensitometer trace taken from such an image of the focal spot produced by a 100:1 aspect ratio RPP (elements are $a = 10$ mm by $b = 100$ μm; the near-field laser beam is circular and 10 cm in diameter). The image was recorded in the tight focus plane ($z_i = f$) of an $f = 1/4$ m lens. Figure 1(b) shows the profile predicted by the interference code for this RPP–lens combination. In the calculation the number of RPP elements contributing to the intensity pattern was limited to 50 with two steps per element [that is, $(50 \times 2) \times (50 \times 2)$ grid units] on a total 120×120 input grid. (The outer points are zero.) Larger input grids proved prohibitively costly in terms of computer memory. The particular gridding described was used to achieve suitable spatial dimensions in the focal plane. These are fixed for a discrete Fourier transform by the dimensions of the input gridding [$\Delta x_i = \lambda z_i/N\delta$, where Δx_i is the spatial resolution in the focal plane, N (of the $N \times N$ array) is the total number of grid points along one axis (in this case $N = 120$), $\lambda = 1/4$ μm, $z_i = f, f = 1/4$ m, and $\delta = 50$ μm is the step size of the grid in the near field]. Figure 1(c) and 1(d) show the predicted intensity profile for a 5:1 aspect ratio RPP, where it was possible to simulate a greater number of RPP elements (500). Through a series of comparisons,[6] which are additional to the one in Figs. 1(a) and 1(b), the code is found to predict focal spot intensity profiles accurately.

IV. Production of the Square-Topped Line Focus

It is evident from Fig. 1 that the average intensity profile is approximately sinc^2 in shape. For some important applications, however, it is preferable (or even essential) for the line foci to be more square-topped. This includes the case of line foci for x-ray laser applications, where the plasma conditions along the length of the focus are ideally uniform (to provide uniform refraction and maximal gain).

To achieve this a triangular input phase grid (where h is the height) such as the one shown in Fig. 2 is added to the RPP phase grid. Figure 3(a) shows the effect of this addition on the intensity profile in the focal plane where $h = 5.85\pi$ rad. Figure 3(b) depicts the focal plane intensity profile with $h = 1.17\pi$ rad, which shows an essentially three-peaked line focus. (The dip between the peaks is Ω 30%.) Figure 3(c) shows a one-dimensional trace from Fig. 3(b) in either direction. In the simulations for Fig. 3 the RPP grid was omitted for clarity. Figure 4 shows the effect of including the RPP grid in the $\varphi(x_o, y_o)$ input phase grid ($h = \pi$). In this case the aspect ratio of the resulting line focus is 2:1. However, it is possible to achieve other aspect ratios by using rectangular RPP elements (with appropriate changes in h), as were used to produce the profiles in Fig. 1. Since in any case the delays introduced by the triangular elements are small ($\simeq \lambda$), no significant

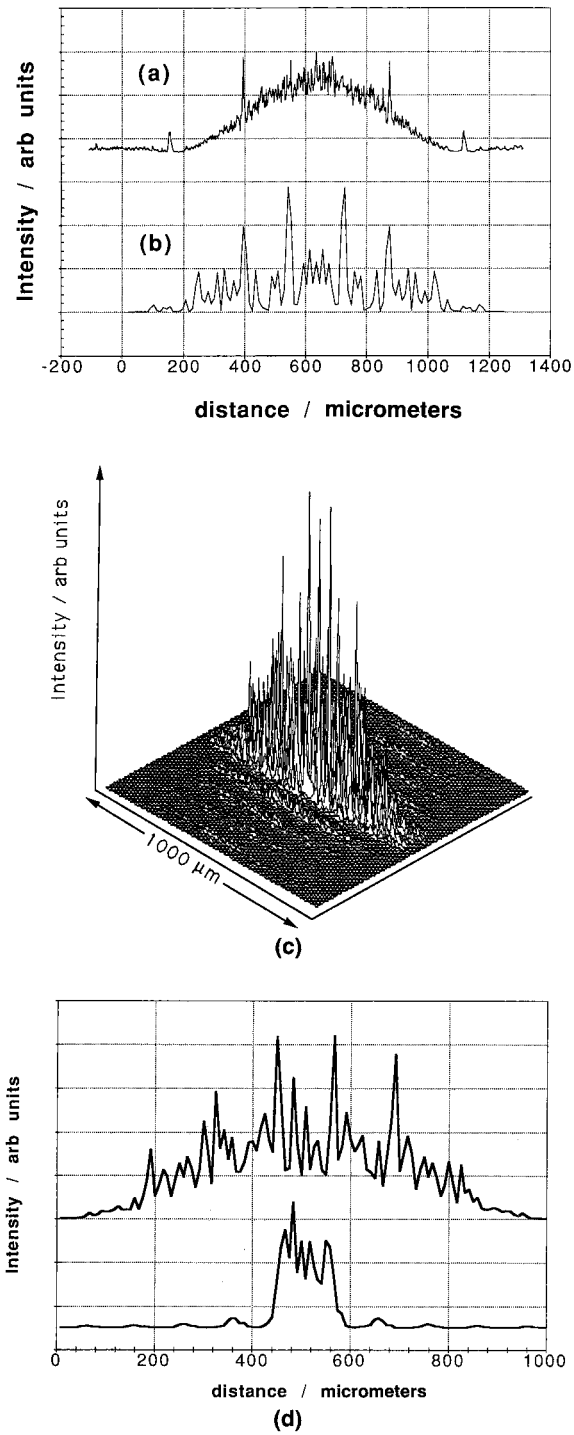

Fig. 1. (a) One-dimensional intensity trace of a focal spot produced by a 100:1 aspect ratio RPP (10 mm × 100 μm elements), 10-cm beam width, $\lambda = 1/4$ μm, and $f = 1/4$ m. (b) One-dimensional intensity trace taken from the interference code simulation for the 10 mm × 100 μm phase plate in focusing conditions that are identical to those in (a). Because of the considerations of image plane dimensions (which are fixed by input plane dimensions for a discrete Fourier transform) and of computer memory space, only 50 RPP elements could be simulated [compared with ~8000 contributing to the focal spot in (a)]. This accounts for the difference between the two plots. (c) Interference code simulation for a 5:1 aspect ratio RPP (5 mm × 1 mm elements), 5-cm beam width, $\lambda = 0.5$ μm, $f = z_i = 1$ m. (d) One-dimensional trace from (c).

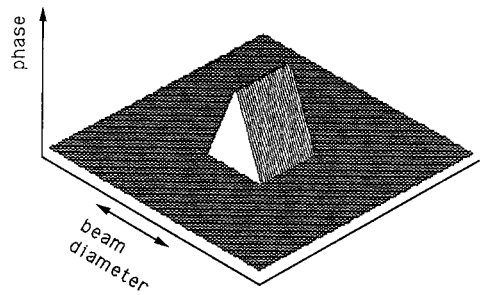

Fig. 2. Triangular phase input grid.

delays are produced across a line focus that is produced by this method (see Section I).

For design purposes it is useful to relate h to the thickness of the glass that is required to produce this phase shift t and to the separation of the two focal spots (in terms of the focal spot width):

$$h = 2\pi(n - 1)t/\lambda, \tag{2}$$

where n is the refractive index of the glass. The physical path difference s is

$$s = (h/2\pi)\lambda. \tag{3}$$

Let Δ be the peak-to-peak separation of the two focal spots that result from the bitriangular phase element. It is convenient to express this in terms of the diffraction-limited zero-to-zero focal spot width, $D = 2f\lambda/a$, where a is the width of the triangular element (in this case this is one half of the beam width):

$$\Delta = kD, \tag{4}$$

where k is a constant. From geometrical optics

$$s/a = (\Delta/2)/f. \tag{5}$$

Combining Eqs. (3), (4), and (5) one obtains

$$h = 2\pi k. \tag{6}$$

By using Eq. (6) the optimal value of k [which produces the profile in Fig. 3(b), $h = 1.17\pi$] is 0.58, so that $\Delta = 0.58D$ [from Eq. (4)]. When a square-element RPP is used in addition (Fig. 4) the optimal value of k is slightly lower at 0.5 ($h = \pi$, $\Delta = D/2$, a = width of RPP elements = 4 mm). This difference in the optimal values of k for the two cases (Figs. 3 and 4) arises because the average intensity profiles are not identical.

Bitriangular elements such as the ones that we propose could be manufactured by the same lithographic technique as is used currently to make RPP's.[7] This involves introducing a neutral density wedge into the photoresist-illumination stage of the lithographic process to generate the triangular phase front. Alternatively, the required gradient could be applied at the plastic deposition stage by continuously (or in discrete steps) varying the deposition thickness

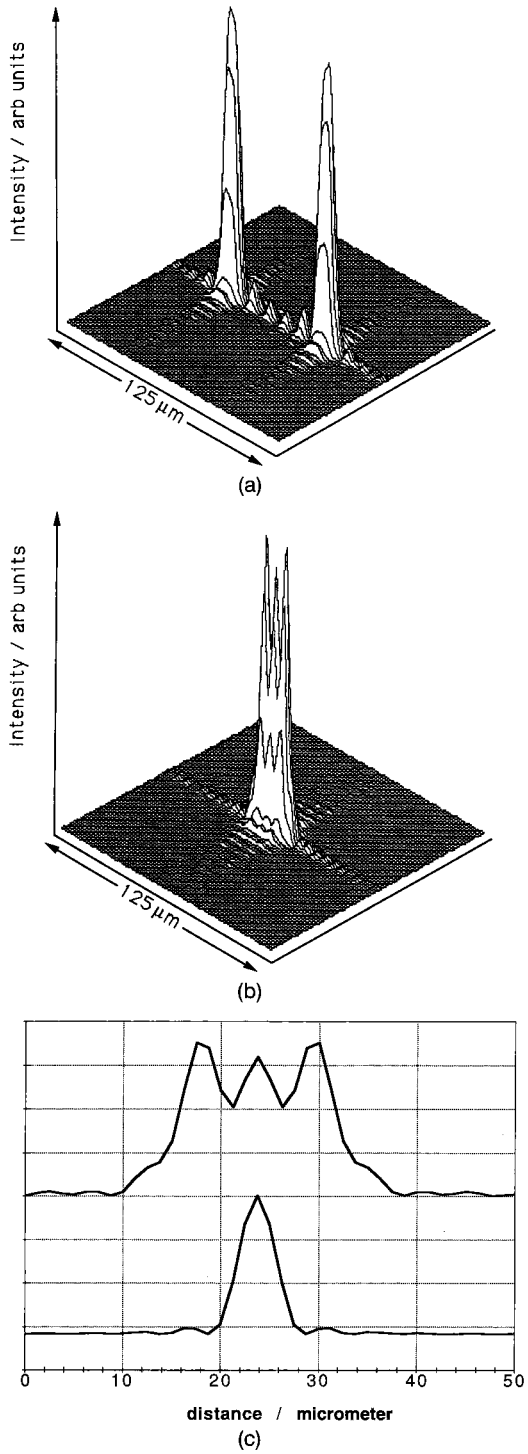

Fig. 3. (a) Effect of using a triangular phase input function on the focal spot profile (no RPP). (Conditions: $h = 5.85\pi$, $\delta = 4$ mm, $N = 26$ on a total grid of 100×100, $f = z_i = 1$ m, $\lambda = 0.5$ μm, beam width 10 cm.) (b) Same conditions as for (a) with $h = 1.17\pi$. (c) One-dimensional scans from (b) in either direction showing an $\simeq 30\%$ dip between the peaks.

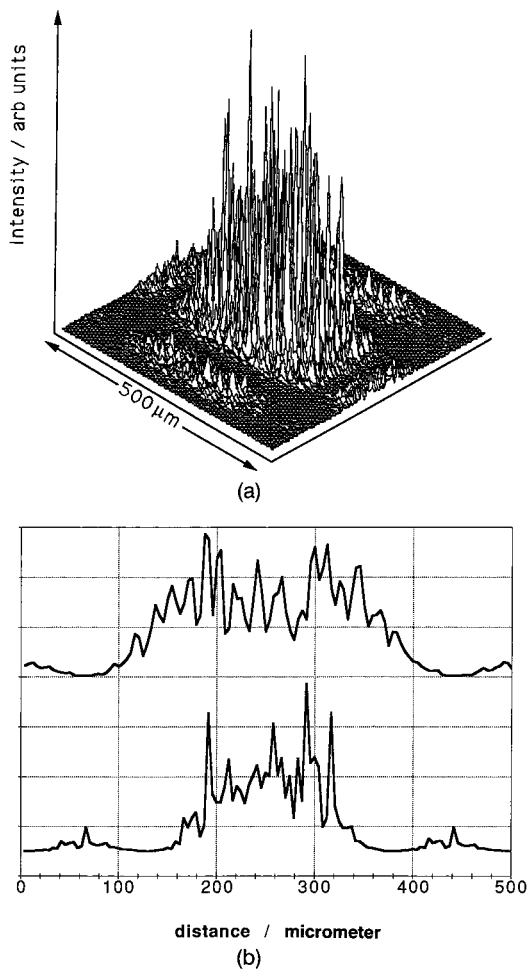

Fig. 4. (a) Effect of adding square RPP elements to the triangular phase input function. (Conditions: $h = \pi$, $\delta = 1$ mm, $N = 100$ on a total grid of 120×120, $f = z_i = 1$ m, $\lambda = 0.5$ μm, beam width 10 cm, a = width of RPP elements = 4 mm). (b) One-dimensional scans from (a) in either direction (averaged over 20 μm) showing a more square-topped intensity profile than in, for example, Figs. 1(a) and 1(b). Again the computations were limited to a low number of RPP elements by the required image plane dimensions (see the caption for Fig. 1).

across the plate. The reverse side of the substrate could be used for the RPP elements. Alternatively, the substrate could be polished at the appropriate angles. High-power holographic emulsions on optically flat substrates could be used to make holographic copies (by in-line holography) of such a master plate. A different value of h would have to be used, however, for such holographic phase elements; the value for the optimally square intensity profile depends on the efficiency of the hologram (since a certain percentage of the laser light remains in zero order). Another possibility would be to construct a triangular system out of three optical flats and fill the volume trapped with index-matching fluid. If the two tilted flats are free to move about a fixed central axis, the amount of shift could be continuously varied. [Because of the small tilts that are involved the required fluid reservoir would be very small ($\simeq 5$ μL for a 10-cm-diameter beam).]

This system could easily be extended to produce square-topped, square foci by using two orthogonal sets of triangular elements combined with square RPP elements. This would produce effectively four focal spots, which could be made to produce the

desired profile by varying k in each direction. Using this same arrangement with rectangular RPP elements results in a cross-shaped profile. It follows that by varying the RPP elements (examples that are not mentioned include rhombic and circular elements) and the tilt elements and, if required, by introducing other phase shifts in the input plane, it is possible to generate almost any arbitrary focal spot profile.

Another approach to the problem of producing square-topped focal spots seeks to use purely binary RPP patterns to generate these.[7] This method appears to suffer from the problem of substantial error loss in the sidelobes of the far-field diffraction pattern. However, the proposed binary phase fronts have been investigated by using the code,[6] and, but for the losses mentioned, the results show it to be feasible. The losses arise because small-scale elements are used to diffract energy to points outside the central maximum. It should be stated that there are a number of techniques[9] for the binarization of arbitrary profiles, and combining these with the idea of random phasing to reduce laser coherence and (hence spikes in the focal spot) appears to be a promising approach, although further work is needed.

V. Application of Line-Focus RPP to the Production of High-Density Cylindrical Laser Plasmas

The production of hot, high-density cylindrical plasmas with a high aspect ratio is of great relevance in x-ray laser research. In particular, the close to solid initial density that is needed to achieve amplification in the water window[10] by recombination requires the use of short-wavelength heating laser beams[11] of short duration. We have carried out a preliminary study of the production and characterization of a cylindrical plasma by using rectangular-element RPP's to produce line foci.

Solid Al targets were irradiated with the prepulse-free, 12-ps KrF SPRITE (as described in Section III) laser pulse at irradiances above 10^{14} W cm^{-2} in a line focus configuration. The plasma produced was characterized by means of time-resolved extreme UV (XUV) spectroscopy and pinhole camera imaging. A pulse-to-prepulse energy contrast ratio of $> 10^8$ was measured at the output of the Raman amplifiers of this laser system resulting in a power contrast ratio of $> 2 \times 10^{10}$. The laser beam was focused onto planar targets with an $f/2.5$ aspheric doublet lens. An RPP with 10-mm $\times$ 100 μm (100:1) rectangular elements was placed near the main focusing optics to produce a line focus as described in Section III.

The primary plasma diagnostic was a time-resolved XUV spectrometer that used a grazing-incidence flat-field grating coupled to an XUV streak camera.[12] A spectral wavelength window from 10 to 70 Å was explored. The temporal and spectral resolutions were 10 ps and 0.3 Å, respectively. The instrument was positioned at an angle of 45 deg to the incident laser beam in the horizontal plane. The size and uniformity of the focal spot were monitored by an x-ray pinhole camera whose line of view was at 35 deg to the line focus axis. Figure 5(a) shows a typical x-ray image with a spatial resolution of ~ 30 μm. The x-ray radiation was filtered by a 25-μm Be foil (x-ray photon energy > 1.5 keV). Densitometer traces of this image are shown in Fig. 5(b). The slight asymmetry of the intensity profile along the x direction of the line focus is a pure geometrical effect caused by the angle of view of the pinhole camera. An experimental aspect ratio of ~ 9 is inferred from this x-ray image. The discrepancy of this ratio from that of the predicted laser focal spot (100:1) is due to the inherent divergence of the laser beam. This was measured to be 120 μrad and thus limits the focal spot width to 30 μm for the 0.25-m focal length lens used. A slight ($\simeq 20\%$) variation in focal spot width is observed on a shot-to-shot basis as a result of thermal effects.

Although the measurements do not allow a complete description of the plasma uniformity that is achieved in the experiment (and hence of the effective-

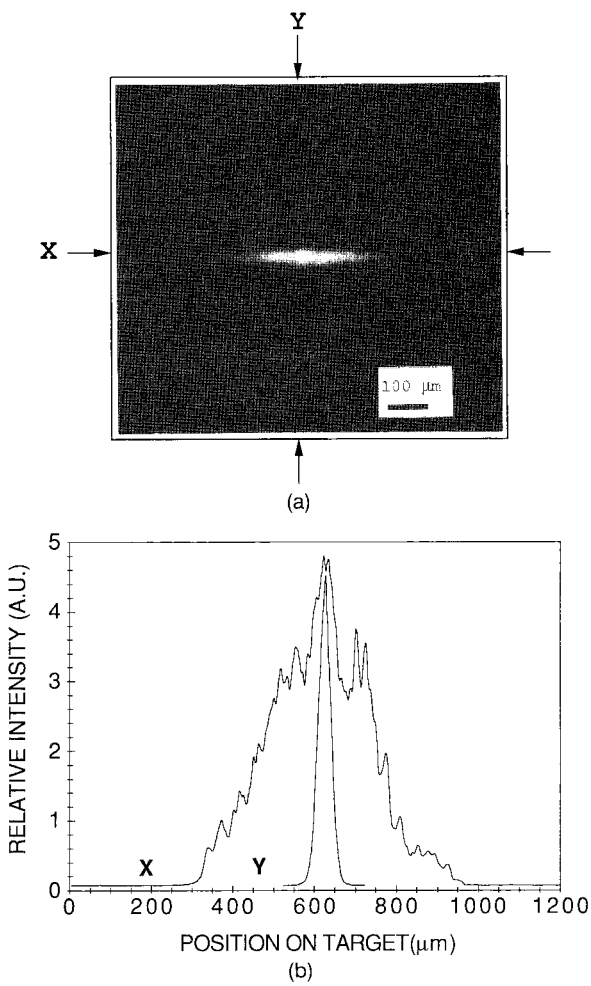

Fig. 5. (a) X-ray pinhole camera image of an Al plasma produced by irradiation of a solid target with a 12-ps, 268-nm KrF laser pulse at an irradiance of 2×10^{14} W cm^{-2}. The radiation was filtered by a 25-μm Be foil. The directions X and Y indicate the lines along which traces are taken in (b). Microdensitometer traces of the x-ray pinhole camera image (a).

ness of the RPP), the data show that a reasonably uniform plasma ($\simeq 10\%$ variations) is observed with a spatial resolution of 30 μm [Figs. 5(a) and 5(b)]. This is incomplete because any nonuniformities existing on a scale length that is shorter than 30 μm would not have been detected. Since the speckle scale of the RPP is 1–2 μm and since lateral smoothing effects are expected to be small (see also Section V.B), it is expected that nonuniformities in the plasma exist on a scale length that is shorter than this. Possible methods of improving the focal spot uniformity include the technique of echelon-free ISI,[13] which would introduce temporal smoothing to the intensity profile produced by the RPP and the SSD technique,[3] where a wavelength-dispersing element is used in combination with an RPP to generate a spatially smoothed profile (owing to the spatially dependent interference of components of different wavelength). A combination of these two methods would ideally be used and would represent temporally incoherent SSD smoothing. Bandwidths as wide as $\Delta\nu \cong 200\ \mathrm{cm}^{-1}$ ($\tau_c \cong 150$ fs) have been achieved with KrF systems,[14] which suggest that both methods could be used effectively even with short ($\simeq 10$ ps) pulse systems.

A. Modeling of Plasma Hydrodynamics and Atomic Physics

The identification of the XUV spectrum was carried out by using a multiconfiguration Dirac–Fock atomic physics code[15] and RATION/SPECTRA[16] numerical codes. Synthetic spectra of hydrogenic, He-like, and Li-like aluminum lines for a given electron density and temperature were generated by RATION. The multiconfiguration Dirac–Fock code was used to calculate the oscillator strength of Be-like aluminum lines, which allow this ionization stage to be included in the analysis. A detailed modeling of the temporal dependence of electron temperature and density profiles was obtained by the one-dimensional Lagrangian hydrodynamics code MEDUSA.[17] In this simulation the laser energy was absorbed through inverse bremsstrahlung. In addition a small portion ($<5\%$) of the energy not absorbed in this process was dumped at the critical surface to simulate anomalous absorption. An electron flux limiter of 0.1 was used in the code as suggested by the analysis of time-resolved x-ray (H-like and He-like Al) spectra taken when a circular focal spot was used to irradiate plastic-coated aluminum targets. Finally a total absorption of $\sim 50\%$ of the input laser energy was accounted for by the code. Figure 6 shows the result of a simulation for the above-mentioned condition of interaction in terms of curves on the T_e–N_e plane at different times relative to the peak of the laser pulse.

A typical output from RATION for given plasma temperature and density as predicted by MEDUSA is shown in Fig. 7. The intensity of the hydrogenic, He-like, and Li-like lines is calculated by the code for a 1-μm plasma size in an optically thick regime where optical depth effects are approximated by escape factors.[18] The value of 1 μm is chosen since this is

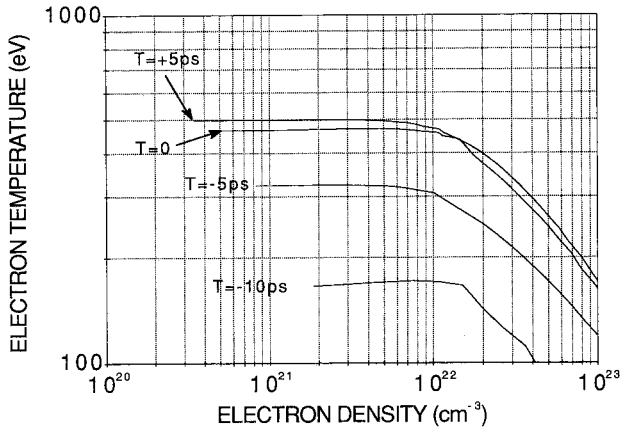

Fig. 6. Evolution of electron density and temperature as predicted by MEDUSA for the interaction of a 12-ps to 268-nm laser pulse with a solid Al target. The result of the simulation is shown in terms of curves on the N_e–T_e plane at different times that are relative to the peak of the pulse. The average irradiance was $2 \times 10^{14}\ \mathrm{W\ cm^{-2}}$.

the distance by which the plasma expands with a typical sound speed of $10^7\ \mathrm{cm\ s^{-1}}$ in a time period of 10 ps. The multiconfiguration Dirac–Fock code was used to determine the oscillator strengths of the main transitions of the Be-like Al to be included in the identification of experimental spectra.

Although the relative intensities of emission lines as calculated by RATION is helpful in the identification of experimental spectra, great care must be taken when attempting to determine plasma conditions by comparison of these intensities with the experimental ones. In fact, as will be pointed out below, the effects of spatial integration of radiation emitted over the whole plasma must be accounted for.

B. XUV Time-Resolved Spectroscopy

A typical time-resolved XUV spectrum of the plasma produced by line focus irradiation of an Al target is shown in Fig. 8(a). The laser energy on target was ~ 1 J resulting in an irradiance of $2 \times 10^{14}\ \mathrm{W\ cm^{-2}}$ at

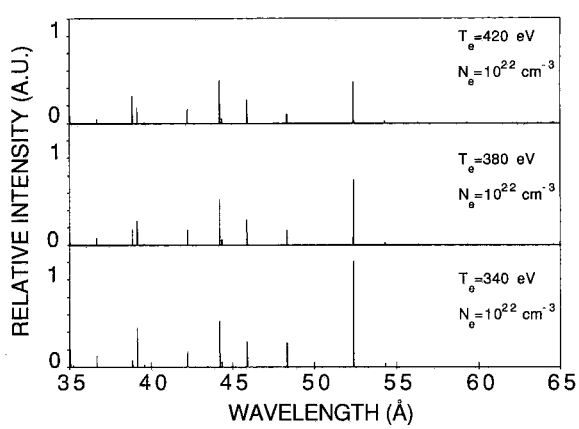

Fig. 7. Synthetic spectrum of XUV emission from an Al plasma at an electron density that is approximately equal to the critical density (at 268 nm) as generated by RATION. The output relative to three different electron temperatures are shown in the same plot.

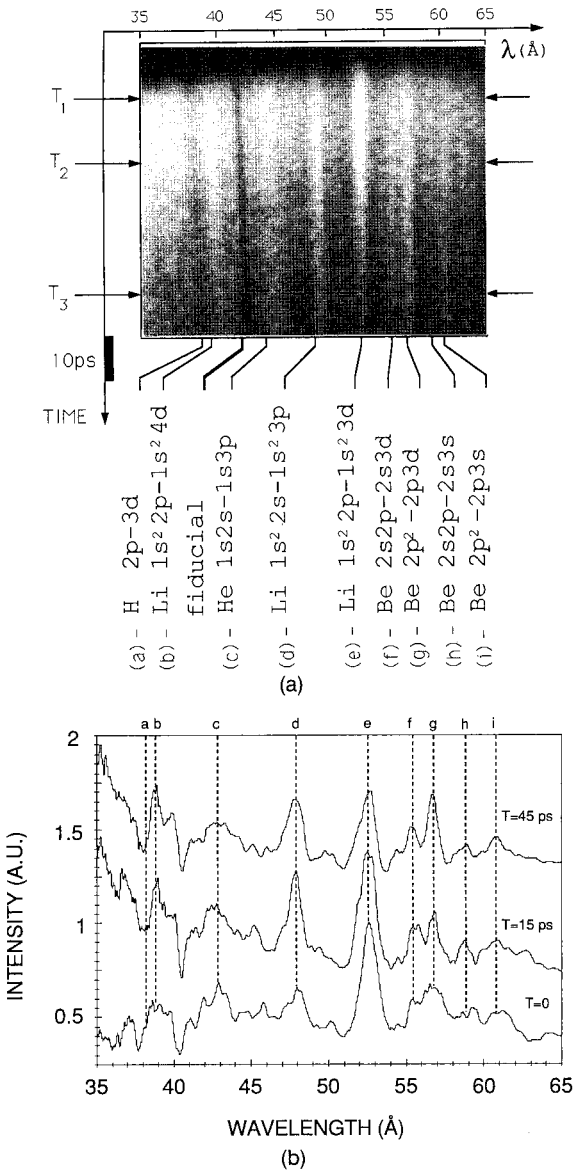

Fig. 8. (a) XUV time-resolved spectrum of radiation emitted by an Al plasma that is produced by the irradiation of a solid target with a 12-ps laser pulse at irradiance of 2×10^{14} W cm^{-2} in a line focus configuration. (b) Densitometric traces of the spectrum (a) at different times with respect to the beginning of the emission as indicated in (a). A different intensity offset has been chosen for each of the traces to avoid overlap.

40 μm × 400 μm. Three microdensitometer traces taken early in the emission and 15 and 45 ps later, respectively, are also given in Fig. 8(b) where transitions originating from hydrogenic to Be-like ions and their temporal evolution are more clearly visible. Electron temperatures and densities between 350 and 400 eV and between 10^{22} and 10^{23} cm^{-3}, respectively, are inferred by the comparison of these traces with the synthetic spectra generated by RATION.

The trace at $T = 0$ in Fig. 8(b) shows the hydrogenic 2p–3*d* Balmer-α line at 38.6 Å partially merged with the strong Li 2*p*–4*d* transition at 39.2 Å. The Balmer-α line cannot be identified in the traces taken later in the emission since a rapid cooling of the plasma has already occurred, and Li-like and Be-like emission dominates the spectrum.

Further information on the plasma can be gained from a deeper analysis of XUV spectra provided that plasma conditions relevant to radiation emitted in this spectral region are identified. In fact, since our measurement is integrated over the whole plasma, the spectrum shown in Fig. 8 results from a convolution over the electron temperature and density profiles present in the plasma along the direction of irradiation. The effect of these temperature and density gradients can be evaluated if the spectral emissivity as the function of plasma parameters is known. The following simple observation gives an idea of the relevance of these effects to XUV spectroscopy and its interpretation.

The distribution of ions with different ionization stages can be calculated by MEDUSA by using an average atom model. This calculation has been performed for the same condition in Fig. 6, and the ion density for the ionization stages from H-like through Be-like has been plotted in Fig. 9 together with the electron temperature profile. The main feature of this plot is the abundance of He-like ions over the whole length of the plasma column. On the other hand, the well-localized concentration of H-like ions as well as Li-like and Be-like ions is predicted by this calculation. Therefore the local value of electron temperature and density should be considered to explain the spectral features of the radiation that is emitted by different ionization stages. Indeed these local values can be significantly different as shown in Fig. 9 where an electron temperature of 450 eV is predicted at the maximum of H-like ion density, whereas the Li-like ion density is maximum at an electron temperature of 180 eV.

A further contribution to spatial integration effects may come from any lateral heat flow that may occur during the interaction. However, a Fokker–Planck simulation for a slightly shorter laser pulse showed that[19] little lateral flow of energy actually occurs.

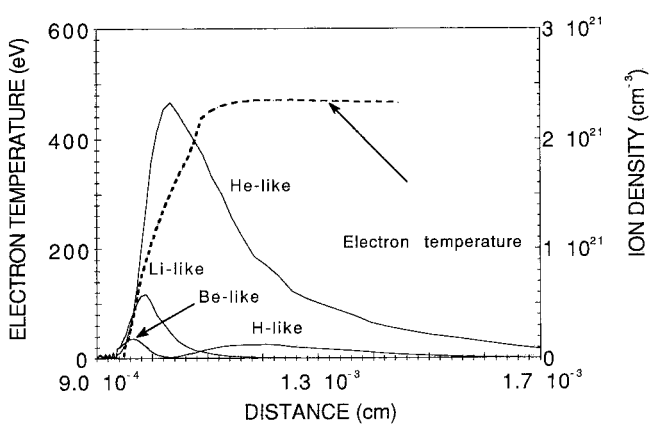

Fig. 9. Ion density distribution for H-, He-, Li-, and Be-like ions predicted by MEDUSA in the same condition of irradiation of Fig. 6. The electron temperature is also plotted (dashed curve).

VI. Conclusions

In conclusion the possibility of employing rectangular-element RPP's for the production of high-aspect-ratio line foci has been investigated both experimentally and with interference code simulations. It is predicted that a square-topped profile can be achieved by adding a small bitriangular phase shift to the RPP system, and the design equations for this are presented. The method of combining such tilt elements with RPP elements of various shapes can be used to achieve almost any focal spot geometry. A rectangular-element RPP was used to generate a cylindrical plasma by using a 12-ps KrF laser pulse. The irradiance achieved was $\sim 2 \times 10^{14}$ W cm^{-2} in a 40 μm × 400 μm focal spot, and the plasma thus produced was found to be uniform on a spatial scale of 30 μm. The plasma conditions were determined by time-resolved XUV spectroscopy, and it is found that suitable conditions for the study of the H-like recombination x-ray laser scheme are produced.

We thank the Central Laser Facility staff, in particular the SPRITE team where these experiments were carried out.

References

1. Y. Kato, K. Mima, N. Miyanaga, S. Arinaga, Y. Kitagawa, M. Nakatsuka, and C. Yamanaka, "Random phasing of high power lasers for uniform target acceleration and plasma instability suppression," Phys. Rev. Lett. **53,** 1057–1060 (1984).
2. R. H. Lehmberg and S. P. Obenschain, "Use of induced spatial incoherence for uniform illumination of laser fusion targets," Opt. Commun. **46,** 27–31 (1983).
3. S. Skupsky, R. W. Short, T. Kessler, R. S. Craxton, S. Letzring, and J. M. Soures, "Improved laser-beam uniformity using the angular dispersion of frequency-modulated light," J. Appl. Phys. **66,** 3456–3462 (1989).
4. R. C. Elton, *X-Ray Lasers* (Academic, San Diego, Calif., 1990).
5. M. Born and E. Wolf, *Principles of Optics* (Pergamon, New York, 1985), Chap. 8, pp. 370–458.
6. M. Desselberger and O. Willi, "Measurement and analysis of Rayleigh–Taylor instability in targets driven by incoherent laser light," submitted to Phys. Fluids. B. M. Desselberger, "Studies of hydrodynamic stability in targets driven by incoherent laser radiation," Ph.D. dissertation. (University of London, London, 1991), Chaps. 2 and 3.
7. C. N. Danson, R. Bann, D. Pepler, I. Ross, J. Exley, D. Hardie, and S. Sails, "Development of random phase plate smoothing technology," Rutherford Appleton Laboratory Rep. RAL-91-025 (Rutherford Appleton Laboratory, Didcot, Oxon, UK, 1991), pp. 62–65.
8. J. R. M. Barr, N. J. Everall, C. J. Hooker, I. N. Ross, M. J. Shaw, and W. T. Toner, "High energy amplification of picosecond pulses at 248 nm," Opt. Commun. **66,** 127–132 (1988).
9. J. C. Stoffel and J. F. Moreland, "A survey of electronic techniques for pictorial image reproduction," IEEE Trans. Commun. **TOC-29,** 1898–1925 (1981).
10. R. A. Smith, V. Barrow, J. Edwards, G. Kiehn, and O. Willi, "High density plasmas for recombination x-ray lasers," Appl. Phys. B **50,** 187–192 (1990).
11. M. D. Rosen, "Plasma physics issues in laboratory x-ray lasers," Phys. Fluid B **2,** 1461–1466 (1990).
12. G. Kiehn, O. Willi, A. Damerell, and M. Key, "Novel time-resolved VUV spectrograph for x-ray laser research," Appl. Opt. **26,** 425–426 (1987).
13. R. H. Lehmberg and J. Goldhar, "Use of incoherence to produce smooth and controllable irradiation profiles with KrF fusion lasers," Fusion Technol. **2,** 532–534 (1987).
14. N. A. Kurnit and S. J. Thomas, "Advanced front-end development," in *Inertial Confinement Fusion at Los Alamos,* 1st ed. (Los Alamos National Laboratory, Los Alamos, N.M., 1989), Vol. 1, Chap. VII.
15. I. P. Grant, B. J. McKenzie, P. H. Norrington, D. F. Mayers, and N. C. Pyper, "Multi-configuration Dirac–Fock calculations of atomic structure," Comput. Phys. Commun. **21,** 207–213 (1980).
16. R. W. Lee, B. L. Whitten, and R. E. Stout II, "Spectra—a model for K-shell spectroscopy," J. Quant. Spectrosc. Radiat. Transfer **32,** 91–101 (1984).
17. J. P. Christiansen, D. E. F. T. Ashby, and K. V. Roberts, "MEDUSA—a one-dimensional laser fusion code," Comput. Phys. Commun. **7,** 271–287 (1974).
18. D. Mihalas, *Stellar Atmosphere* (Freeman, San Francisco, Calif., 1978), Chap. 11.
19. G. J. Rickard, A. R. Bell, and E. M. Epperlein, "2-D Fokker–Plank simulations of short-pulse laser–plasma interaction," Phys. Rev. Lett. **62,** 2687–2690 (1989).